Supplementary Information (SI) for Energy & Environmental Science.
This journal is © The Royal Society of Chemistry 2025

Supporting Information

Polyphosphonitrile Derivative-Based Gel Electrolytes for All-Climate Zinc Metal Batteries Operating from −70 °C to +80 °C

Ran Han, Yuefeng Meng, Xin Zhao, Yao Wang, Mingkun Tang, Yichen Ding, Baohua Li, Dong Zhou, Feiyu Kang*

Electrolyte Preparation: Zinc trifluoromethanesulfonate ($Zn(OTf)_2$, TCI, 99%), methanol (MeOH, Meryer, 99.8%), 1,2-dimethoxyethane (DME, DoDoChem, 99.9%), hexachlorocyclotriphosphazene (HCCP, 98%, Alfa), sodium hydride (NaH, 90%, Sigma-Aldrich), isopropyl alcohol (IPA, Macklin, ≥99.5%), tetrahydrofuran (THF, 99.9%, Acros), isopropyl alcohol (Aladdin, ≥99%), ethyl acetate (EA, Aladdin, ≥99.5%), V_2O_5 (ThermoFisher, ≥99.6%), sucrose (Aladdin, ≥99.5%), 3-butene-1-ol (TCI, 98%), bis[2-(methacryloyloxy)ethyl]phosphate (MEMP, Macklin), 2-hydroxy-2-methylpropiophenone (HMPP, Sigma-Aldrich, 97%), magnesium sulfate ($MgSO_4$, Aladdin, ≥99.5%), PANI (Aladdin, Emeraldine base), poly(tetrafluoroethylene) (PTFE, canrd), N-methyl-2-pyrrolidone (NMP, anhydrous, 99.9%, Sigma-Aldrich), Zn foil (100 μm thickness, 99.9%) and titanium (Ti) foil (10 μm thickness, 99.6%) were purchased from Kluthe. LMP solutions of 1 M $Zn(OTf)_2$ with MeOH and deionized water in volume ratio of 9: 1 was named as MeOH electrolyte. To prepare the gel electrolyte, 5 wt% BCPN monomer, 1 wt% MEMP crosslinker and 1 wt% HMPP initiator were co-dissolved in MeOH electrolyte as precursor. After that, the precursor solution was injected to a glass fiber membrane (Whatman, GF/A, 260 μm) and exposed to ultraviolet (UV) irradiation (irradiation peak intensity: 860 mW cm^{-2}) for 4 min to get the gel. The DME-based gel electrolyte was prepared following the same procedure except for using DME as the co-solvent.

Synthesis of the BCPN:

The BCPN monomer was synthesized based our previous report.[1] NaH (1.96 g, 81.6 mmol) was first dispersed in 50 ml of freshly distilled THF. Subsequently, 3-butene-1-ol (5.99 g, 81.6 mmol) was added drop-wise under an ice bath to form a sodium alkoxide solution, followed by a drop-wise addition of THF solution of HCCP (4.63 g HCCP in 50 ml THF). The resultant reaction mixture was refluxed overnight at room temperature under Ar atmosphere. After that, the solvent was removed by rotary evaporation. The residue was partly dissolved by a mixture of 150 ml hexane and 30 ml EA, then washed with 300 ml deionized water for three times to remove the NaCl. The organic phase was dried overnight with anhydrous $MgSO_4$ and filtered, and finally BCPN as viscous liquid was obtained by rotary evaporation to remove the residual solvents.

Electrolyte characterizations: The ionic conductivities of the electrolyte samples were recorded using a conductivity meter (FE38-Standard, METTLER TOLEDO) at different temperatures. Static contact angles of different electrolytes on Zn foils were carried out through a contact angle meter (MDTC-EQ-M07-01). DSC was detected by DSC analyzer (DSC, America, Q2000) under a nitrogen atmosphere from −85 to 20 °C with a heating rate of 10 °C min^{-1}. Raman spectra were conducted using a miniature laser confocal Raman spectrometer (Horiba LabRAM HR800, France) with a 532 nm laser at room temperature. ^1H nuclear magnetic resonance spectra (NMR) were recorded on a Bruker Advance III 400 spectrometer using D_2O as the solvent. Fourier transform infrared spectroscopy (FTIR) results were collected by Bruker Vertex 70 FTIR spectrophotometer. For the self-extinguishing time (SET) test in the flammability assessment, 2 g electrolyte was placed on a dish and then torched on fire for more than 5 s. The time required for the flame to self-extinguish was recorded and normalized to the electrolyte mass, providing the SET value in s g^{-1}.

Electrochemical characterizations were tested using CR 2032 coin-type cells. Zn||Zn symmetric cells were assembled using Zn foils (100 μm thick) as electrodes. Tafel plots were measured by scanning between -0.2 and 0.2 V at 1 mV s^{-1}. Chronoamperometry (CA) curves were measured at a fixed potential of -150 mV. Electrochemical impedance spectroscopy (EIS) was implemented using a VMP3 electrochemical workstation within the range of 10^5 to 10^{-2} Hz and an amplitude of 5 mV. The activation energy (*Ea*) for the charge transfer process on the Zn surface was measured

by EIS at different temperatures (from 30 to 70 °C) in Zn||Zn symmetrical cells. The *Ea* was calculated based on the Arrhenius equation:

$$R_{ct}^{-1} = A\exp(-E_a/RT) \quad (1)$$

where R_{ct}, T, R, and *A* represent charge-transfer resistance, absolute temperature, standard gas constant, and preexponential constant, respectively. The hydrogen evolution reaction potential and oxygen evolution reaction potential were recorded using the linear sweep voltammetry (LSV) method with a scan rate of 1 mV s^{-1}. Zn||Cu asymmetric cells were assembled using Zn foil as the anode and Cu foil (9 μm thick) as the cathode.

The crystal structure of the cycled electrodes was detected by X-ray diffraction (XRD; Bruker D8 Advance, Cu-K_α, λ=1.5418 Å). In situ optical microscopy was obtained by photographing the deposition process on Zn foil in a polytetrafluoroethylene cell with a transparent quartz window with a current density of 5 mA cm^{-2} applied. Three dimensions (3D) measuring laser microscope (kathmatic KC-1000) was operated to achieve the confocal laser scanning microscopy images of the Zn surface. The surface roughness and charge distribution of the Zn anode after cycling were characterized and the contact potential difference (V_{CPD}) between the probe tip and the SEl layer were characterized through an atomic force microscope (AFM, MDTC-EQ-M16-01), the electron work function of the SEI layer (φ_{SEI}) is calculated based on the Equation (2):[2]

$$\varphi_{SEI} = \frac{eV_{CPD}}{\Phi_{tip}} \quad (2)$$

Where V_{CPD} is the contact potential between the tip of the probe and the SEI layer, which is the average value of the surface, φ_{tip} is the real value of the electron work function of the platinum probe tip, which is 5.1 eV. The Zn||Zn symmetric cells were subjected to constant current discharge of 1 mA cm^{-2} and 2 mAh cm^{-2} after 10 cycles of stable cycling at 1 mA cm^{-2} and 1 mAh cm^{-2} to obtain the SEI layer on the Zn surface. The Zn foil was then vacuum dried at 60 °C for 2 h before the interfacial SEI modulus test. The test procedure included selecting three points on the test interface to obtain force-displacement curves, and analyzing the SEI modulus of the Zn anode surface based on the approach curve and depart curve curves of different test points and taking the average value.

The localized nanoscale mid-IR spectra and absorption maps were carried out using a Bruker nanoIR3 instrument under contact mode. The surface compositions of cycled Zn foil were characterized by time-of-flight secondary ion mass spectrometry (TOF-SIMS, PHI Nano TOF-2). HR-TEM images of SEI were collected on FEI Tecnai G2 F30. The SEI compositions were investigated by X-ray photoelectron spectroscopy (XPS, ESCALAB 250Xi) equipped with Al K_α X-ray source (2 kV and 6 mA).

Battery fabrication and characterizations: V_2O_5 cathodes were prepared by mixing V_2O_5 powder, acetylene black and PVDF in mass ratios of 7: 2: 1 in NMP to get a uniform slurry, and then pasted onto a Ti foil (10 μm). The cathodes were vacuum dried overnight at 60 ℃ for 12 h and punched into disks. $V_{10}O_{24}{\cdot}12H_2O$ (VOH) cathode material was synthesized following previous studies.[1] Typically, 1 g V_2O_5 and 1 g sucrose were mixed with 70 mL deionized water with 1 h stirring. The yellow solution was transformed to an autoclave with Teflon liner and heated to 100 °C for 12 h. The as-prepared samples were collected and washed with deionized water and ethanol, and then dried at 60 °C in a vacuum oven for 12 h. VOH cathodes were prepared by mixing VOH, acetylene

black and PVDF in mass ratios of 7: 2: 1 in NMP and then pasted onto a Ti foil (10 μm) and vacuum dried at 80 °C for 12 h. The PANI cathodes were obtained by mixing PANI, Ketjen black and polytetrafluoroethylene (PTFE) in an isopropyl alcohol solution in the weight ratio of 6:3.5:0.5, and then pressed onto Ti mesh and vacuum dried for 12 h at 60 °C. ZMB full Cells assembled using the as-prepared V_2O_5, VOH and PANI cathodes, all with a mass loading of 1-2 mg cm^{-2}. First, 100 μL of the precursor solution was added directly to the glass fiber membrane. After in-situ gelation, full cells were then assembled. The cycling test was conducted under 1.5 A g^{-1} with a voltage window of 0.5-1.8 V for Zn||V_2O_5 and Zn||VOH cells at different temperatures, and 0.1 A g^{-1} with a voltage window of 0.4-2.0 V for Zn||PANI cells at LT. The electrochemical performances of the cells were evaluated using the Neware (Shenzhen) battery test system.

For pouch full cells, VOH with a mass loading of ≈2.5 mg cm^{-2} was used as cathode, while Zn foil (100 μm) and glass fiber were used as anode and separator, respectively. The precursor solution injected into the cell was about 30 μL mg^{-1}. The assembled battery was encapsulated in aluminum-plastic film to get pouch cells. X-ray computed tomography (X-ray CT) was carried out on phoenix Vltomelx M instrument. Gas chromatography-mass spectrometer (GCMS, Trace1300-ISQ) was adopted to quantify the gas generation during the reaction. Ultrasonic imaging technology had adopted to non-destructively test the internal changes in the initial and after cycling pouch cells. (Tsing Bosch (Zhuhai) Technology Co., Ltd.).

Theoretical Simulations: Molecular dynamics (MD) simulations were proceeded with Forcite module in Material Studio software.[3-4] The amorphous cells with linear dimensions of 35.0 × 35.0 × 35.0 Å, 36.0 × 36.0 × 36.0 Å, 36.0 × 36.0 × 36.0 Å and 35.6 × 35.6 × 35.6 Å were adopted for MD simulations, corresponding to 1 M $Zn(OTf)_2$, 1 M $Zn(OTf)_2$ in MeOH: H_2O, MeOH electrolyte and gel electrolyte, respectively. The COMPASSIII force field was selected for all molecular dynamics simulations with a fixed time step of 1.0 fs (femtoseconds). After a 1 ns (picosecond) equilibration step in the NPT ensemble using the Berendsen barostat to maintain one standard atmosphere pressure with 0.1 ps decay constant, the statistical averages were calculated from trajectories with a duration of at least 2 ns. The NVT combination was selected and the Nose thermostat was used to control the temperature for MD simulation at 213K, 298K and 333K respectively. The simulation time was long enough to ensure that the electrolyte system was in equilibrium. The partial charges of Zn^{2+} and OTf^- were both scaled by a factor of 0.7 to approximate the effect of charge transfer and polarizability. The cutoff of RDF curves was 0.02 Å. DFT calculations were performed by DMol3 module in Materials Studio software. The geometric optimization calculations and LUMO/HOMO energy levels were carried out with generalized-gradient approximation/Perdew–Burke–Ernzerhof (GGA/PBE) functional and dual numerical polarization (DNP) basis sets. The convergence tolerance was set to 1.0×10^{-5} Ha, 2.0×10^{-3} Ha $Å^{-1}$, and 5.0×10^{-3} Å for energy, maximum force, maximum displacement, and maximum number of iterations, respectively. Zn^{2+}-solvent complexes were constructed by placing Zn atoms near the hydroxy O and water O atoms of solvent molecules, which are atomic centers carrying negative charges. The desolvation energy between the Zn^{2+} and solvent molecules is defined as:[5]

$$E_d = E_{clusters-A} + E_A - E_{cluster} \quad (3)$$

in which $E_{clusters\text{-}A}$, E_A and $E_{clusters}$ represent the total energy of the solvated clusters after the removal of A, free A, and solvated clusters without removing A, respectively.

Supporting Figure and Table

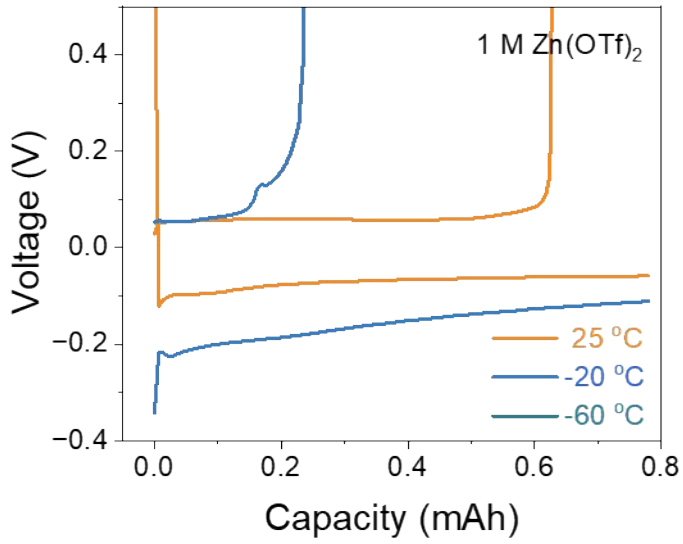

Fig. S1. Initial charge-discharge curves o of Zn||Cu cells within 1 M $Zn(OTf)_2$ aqueous electrolyte at different temperatures at 1 mA cm^{-2}.

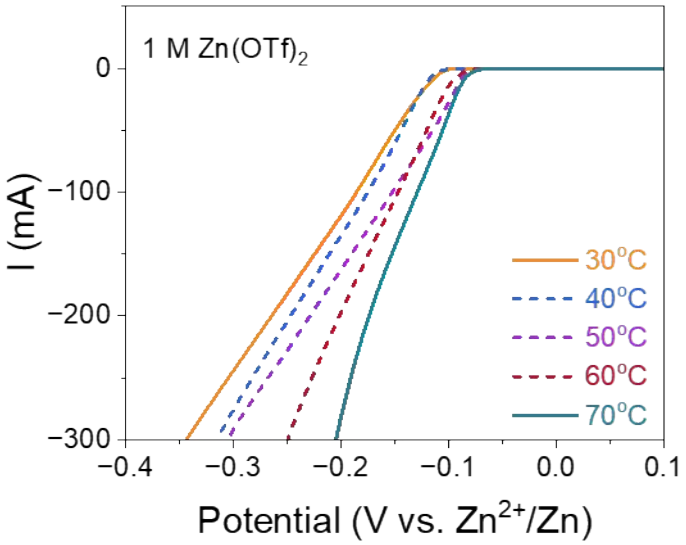

Fig. S2. LSV curves in 1 M $Zn(OTf)_2$ aqueous electrolyte at different temperatures.

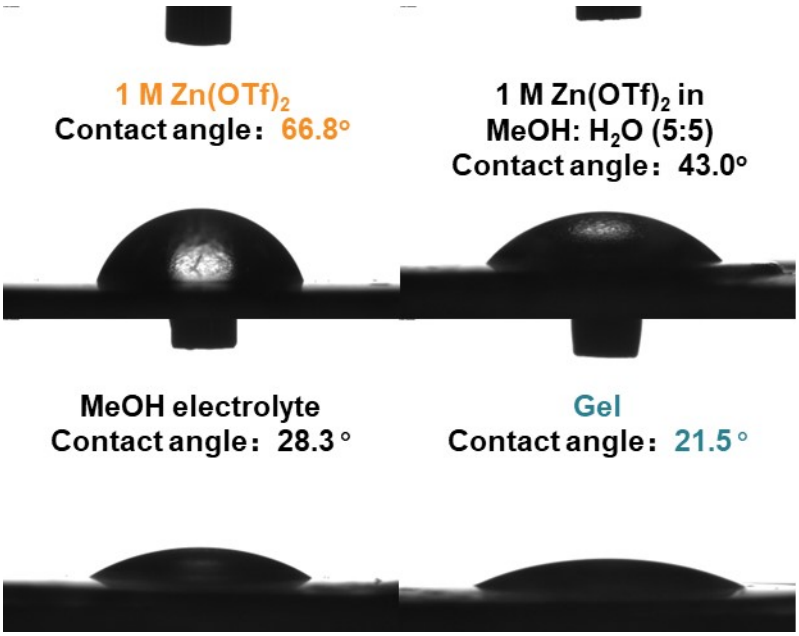

Fig. S3. Contact angle measurement on Zn metal anode with different electrolytes. It is seen that the addition of MeOH reduces the contact angle on Zn metal.

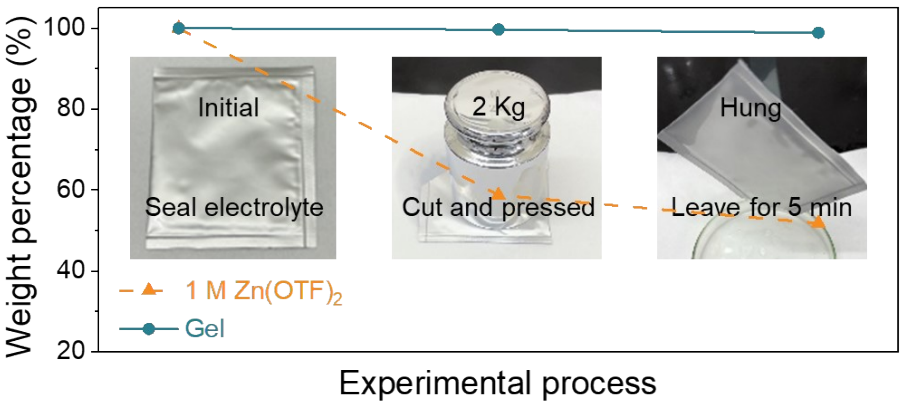

Fig. S4. Leakage tests of 1 M $Zn(OTf)_2$ aqueous electrolyte and gel electrolyte. Visual observation of electrolytes in different leakage states are shown in the insets. The weight loss of a 1 M $Zn(OTf)_2$ aqueous electrolyte after compression and suspension was approximately 48.2%, whereas the gel electrolyte showed negligible weight loss (1.1% only).

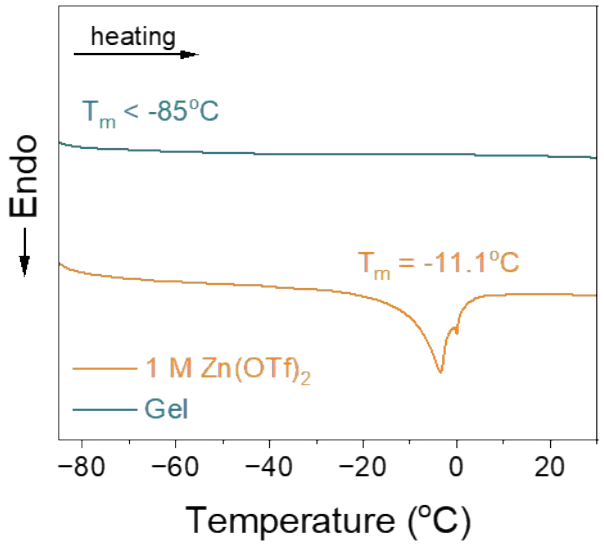

Fig. S5. DSC tests for 1 M $Zn(OTf)_2$ aqueous electrolyte and gel electrolyte from -85 °C to 20 °C.

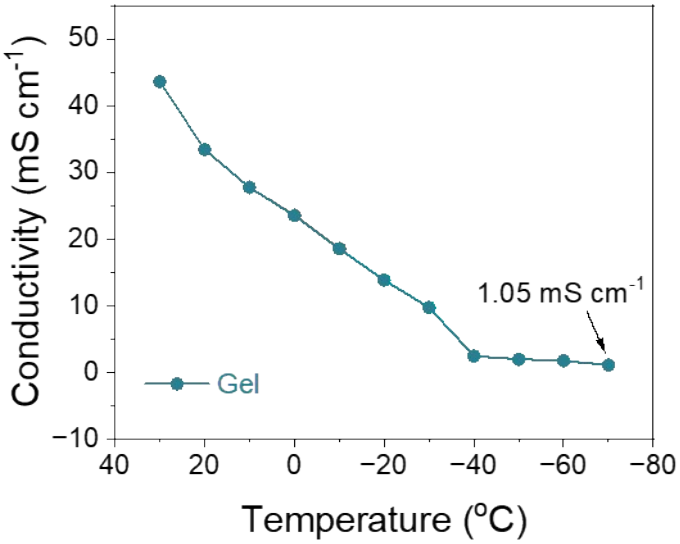

Fig. S6. Ionic conductivities of the gel electrolyte at different temperatures.

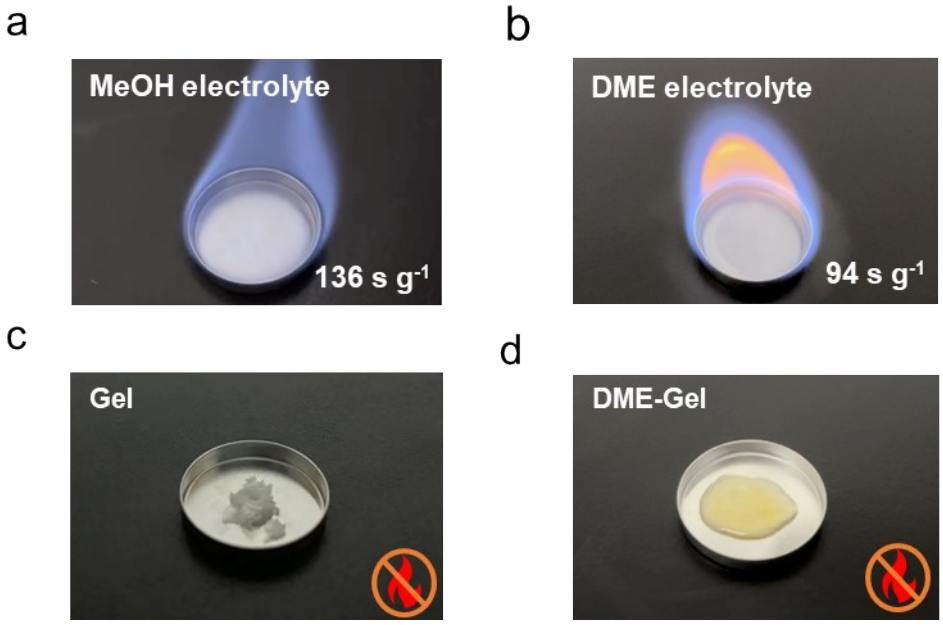

Fig. S7. Combustion tests for two kinds of LMP solvents (upper panels) and corresponding gel electrolytes (lower panels).

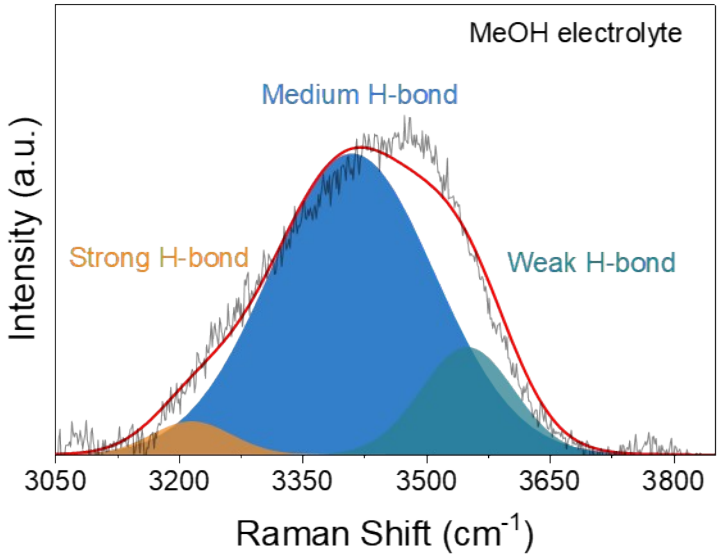

Fig. S8. Raman spectrum for the MeOH electrolyte.

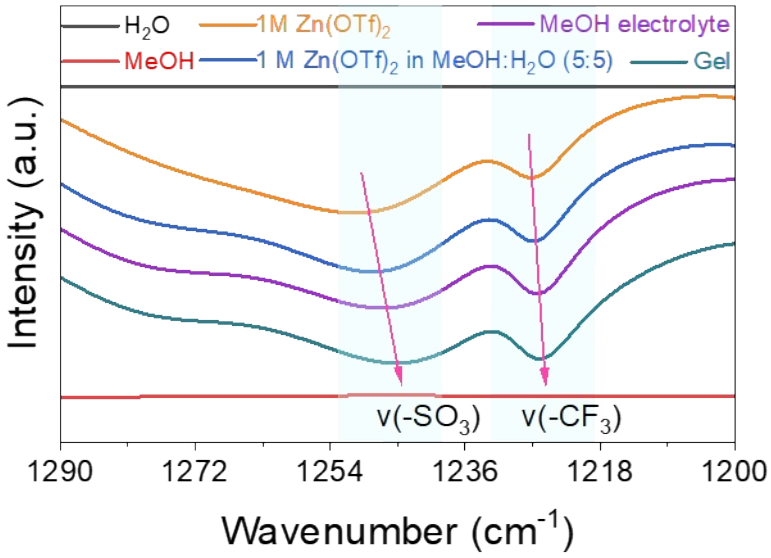

Fig. S9. FTIR spectra of pure H_2O, pure MeOH, 1 M $Zn(OTf)_2$ aqueous electrolyte, 1 M $Zn(OTf)_2$ in MeOH: H_2O (5: 5) electrolyte, MeOH electrolyte and gel electrolyte from 1290 to 1200 cm^{-1}.

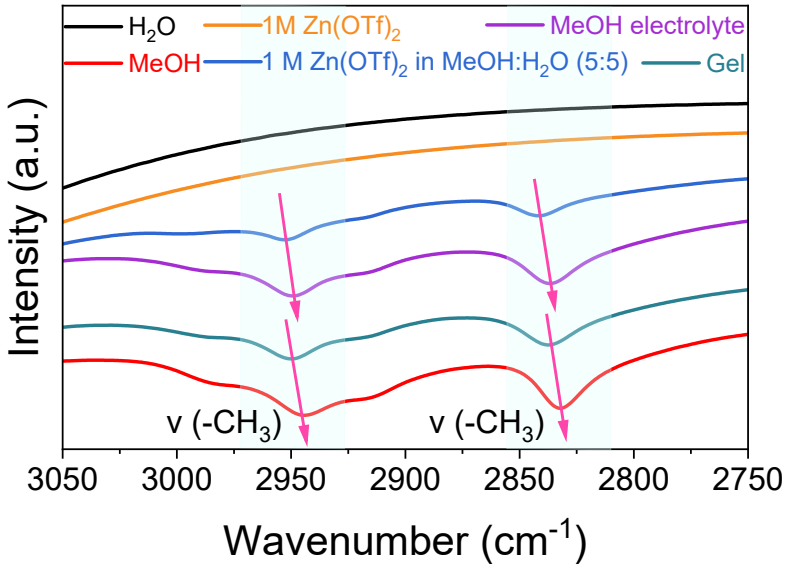

Fig. S10. FTIR spectra of pure H_2O, pure MeOH, 1 M $Zn(OTf)_2$ aqueous electrolyte, 1 M $Zn(OTf)_2$ in MeOH: H_2O (5: 5) electrolyte, MeOH electrolyte and gel electrolyte from 1050 to 1000 cm^{-1}. Peaks at 2945 cm^{-1} and 2833 cm^{-1}, corresponding to asymmetric and symmetric stretching vibrations of MeOH, respectively.

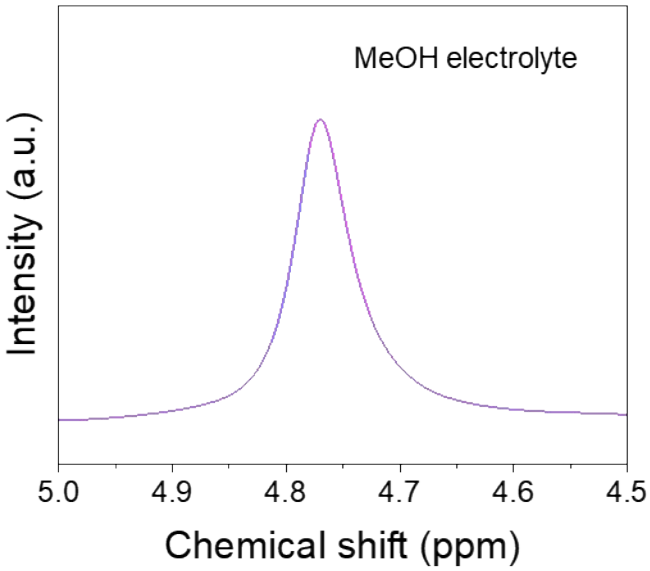

Fig. S11. ^{1}H NMR spectra for the MeOH electrolyte.

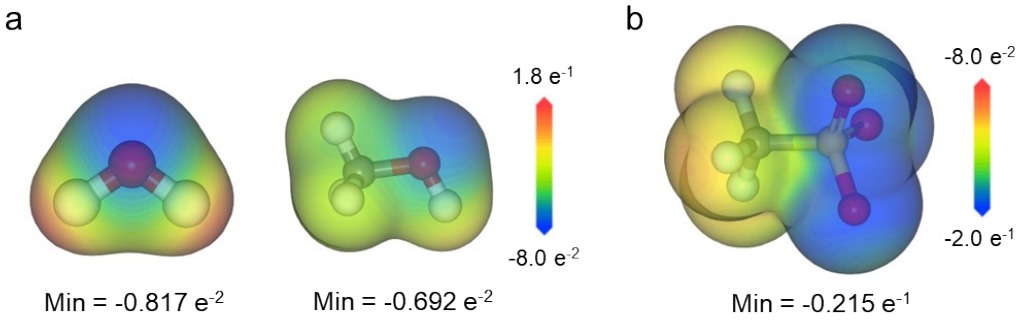

Fig. S12. ESP mappings of molecules structures. (a) H_2O and MeOH. (b) OTf^- anion. Color code: O, red; F, cyan; C, dark gray; S, yellow and H, white. It is seen that OTf^- exhibits the lowest ESP value (-0.215 e^{-1}), with the negative charge primarily localized on the -SO_3 functional group, making it preferentially coordinate with Zn^{2+}. In contrast, H_2O (-0.817 e^{-2}) and MeOH (-0.692 e^{-2}) molecules exhibit relatively similar ESP values, with the negative charge mainly concentrated on the oxygen atoms.

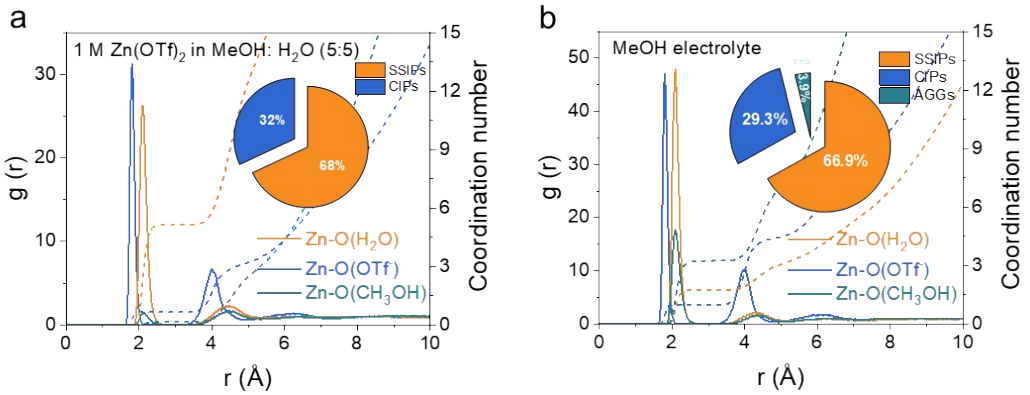

Fig. S13. RDFs and the coordination numbers between Zn^{2+} and H_2O, OTf^- and MeOH in (a) 1 M $Zn(OTf)_2$ in MeOH: H_2O (5:5) electrolyte and (b) MeOH electrolyte. The proportions of SSIP, CIP and AGG in different electrolytes are shown in the insets.

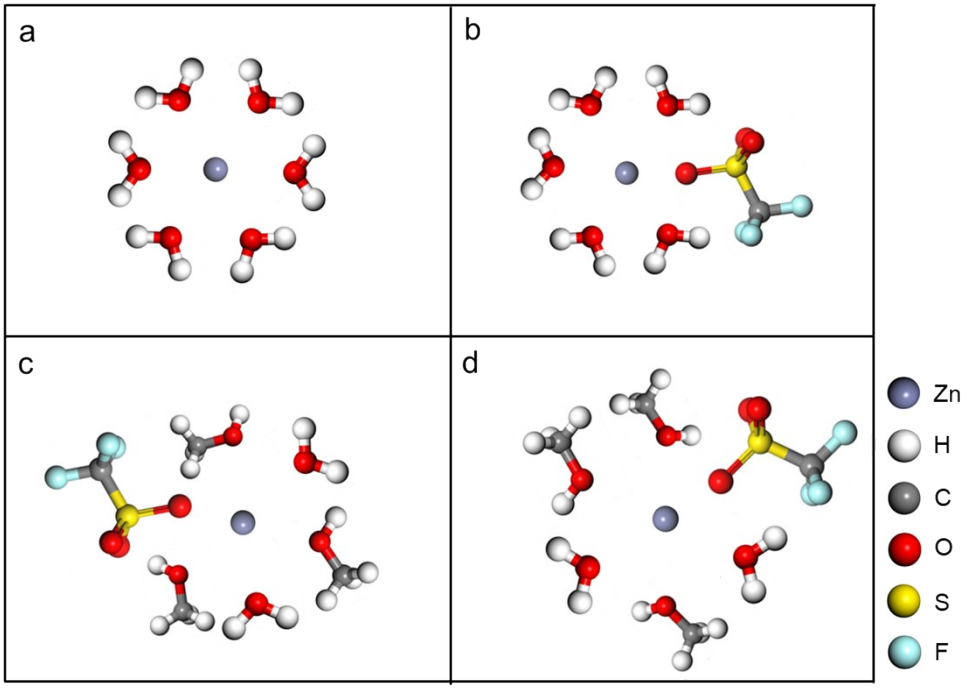

Fig. S14. Structural schematic diagram of the first solvation sheath of Zn^{2+} for (a) 1 M $Zn(OTf)_2$ aqueous electrolyte, (b) 1 M $Zn(OTf)_2$ in MeOH: H_2O (5:5), (c) MeOH electrolyte, and (d) gel electrolyte, respectively.

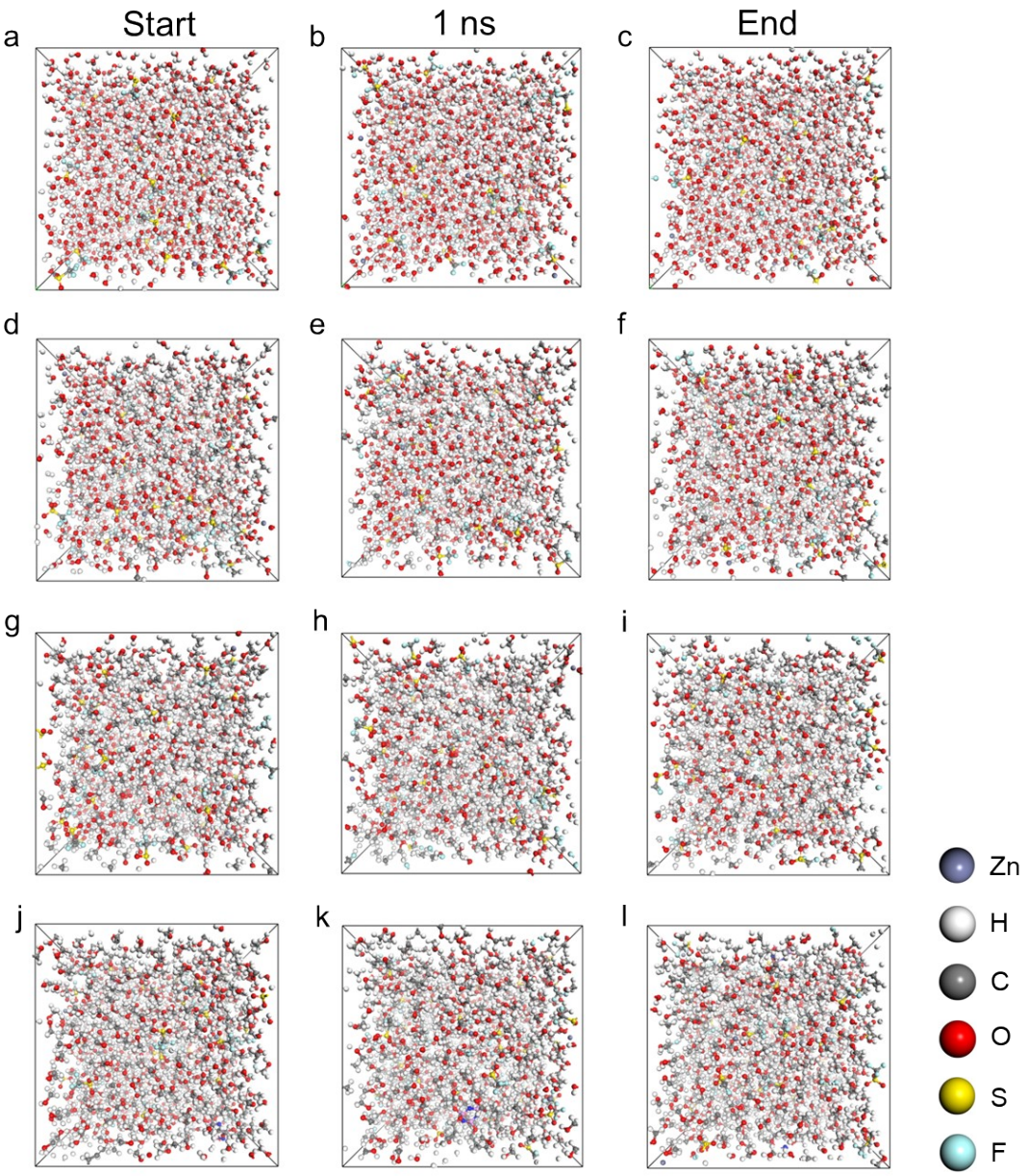

Fig. S15. 3D snapshots of (a-c) 1 M $Zn(OTf)_2$ aqueous electrolyte, (d-f) 1 M $Zn(OTf)_2$ in MeOH: H_2O (5: 5 by volume), (g-i) MeOH electrolyte, and (j-l) gel electrolyte at the start frame, 1ns, and end frame, respectively.

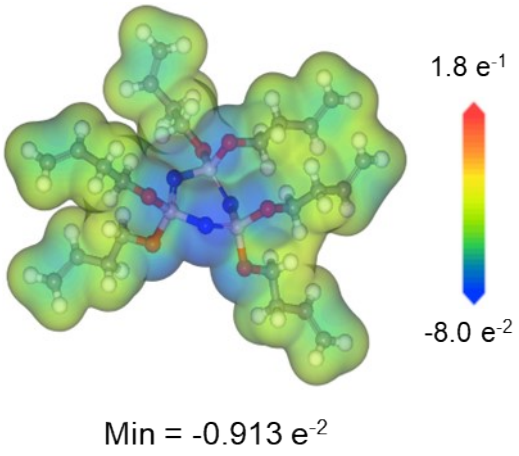

Fig. S16. ESP mapping of BCPN molecule structure. Color code: O, red; N, dark blue; C, dark gray; P, pink and H, white.

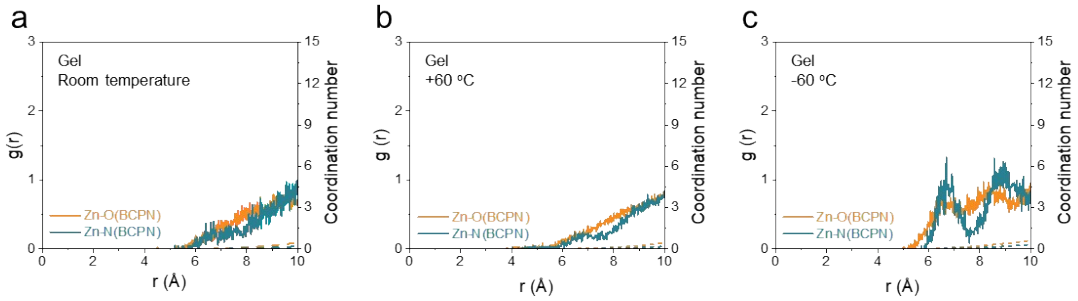

Fig. S17. RDFs and the coordination numbers between Zn^{2+} and O or N in the BCPN molecules in the gel electrolyte at (a) room temperature, (b) +60 °C and (c) -60 °C.

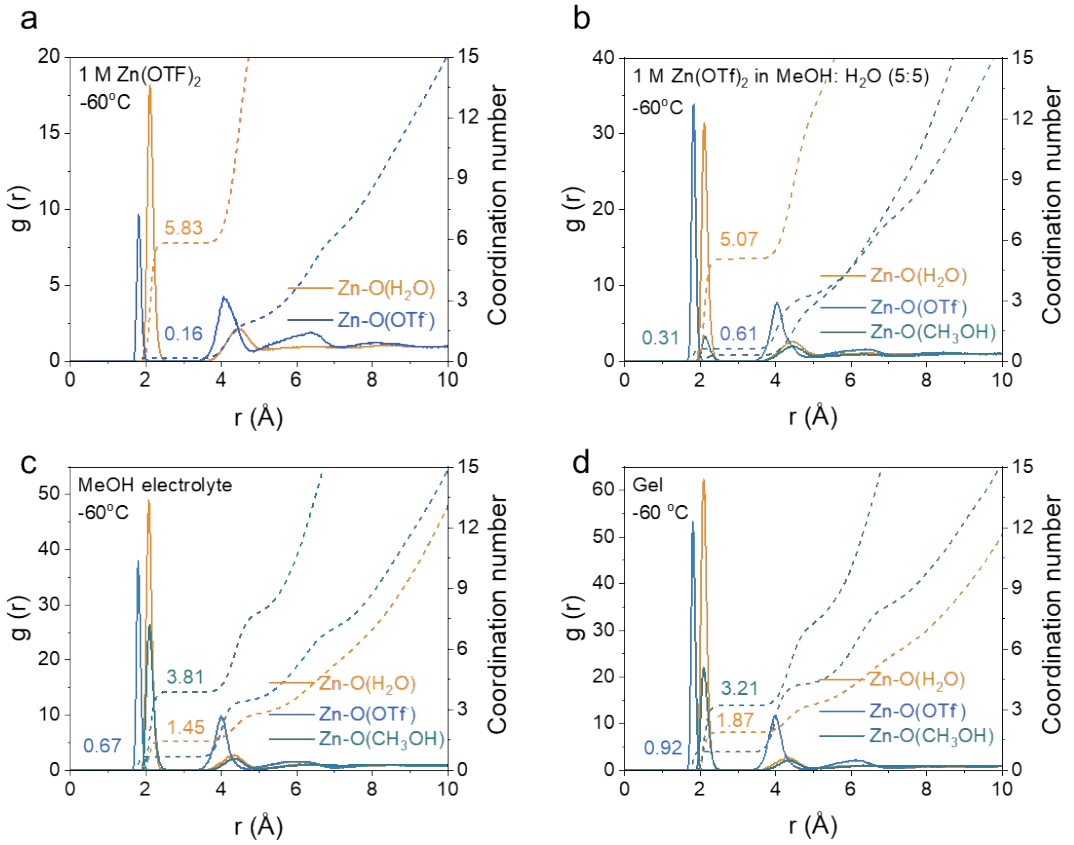

Fig. S18. RDFs and the coordination numbers between Zn^{2+} and H_2O, OTf^- and MeOH in (a) 1 M $Zn(OTf)_2$, (b) 1 M $Zn(OTf)_2$ in MeOH: H_2O (5:5) electrolyte , (c) MeOH electrolyte and (d) gel electrolyte at -60 °C. The coordination number between Zn^{2+} and water in the 1 M $Zn(OTf)_2$ in MeOH: H_2O (5:5) electrolyte is as high as 5.07, indicating that the introduction of a small amount of MeOH cannot effectively alter the first solvation sheath of Zn^{2+}. Therefore, the bulk electrolyte still contains a significant amount of strong hydrogen bonds, stabilizing the hydrogen bond network and ultimately limiting the LT performance of ZMBs. In contrast, in the MeOH electrolyte and gel electrolyte, the coordination numbers between Zn^{2+} and MeOH molecules are higher than that with H_2O molecules, even exceeding the coordination number observed at room temperature.

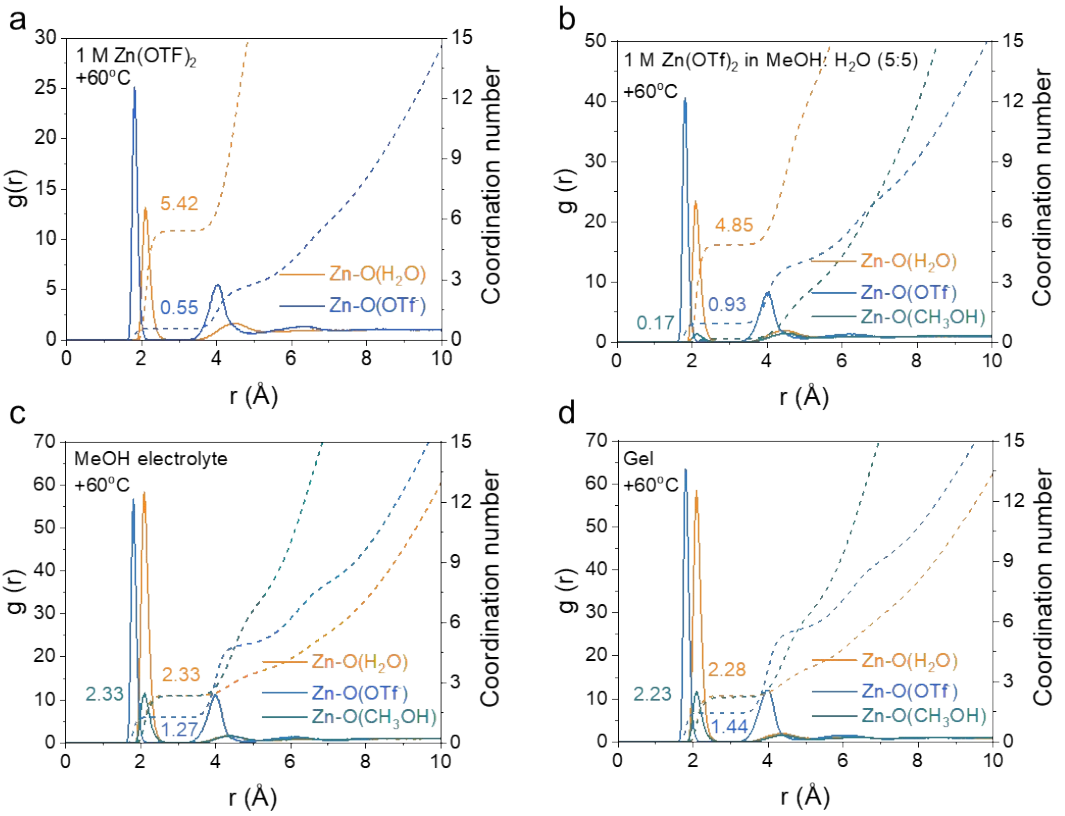

Fig. S19. RDFs and the coordination number between Zn^{2+} and H_2O, OTf^- and MeOH in (a) 1 M $Zn(OTf)_2$, (b) 1 M $Zn(OTf)_2$ in MeOH: H_2O (5: 5) electrolyte, (c) MeOH electrolyte and (d) gel electrolyte at +60 °C.

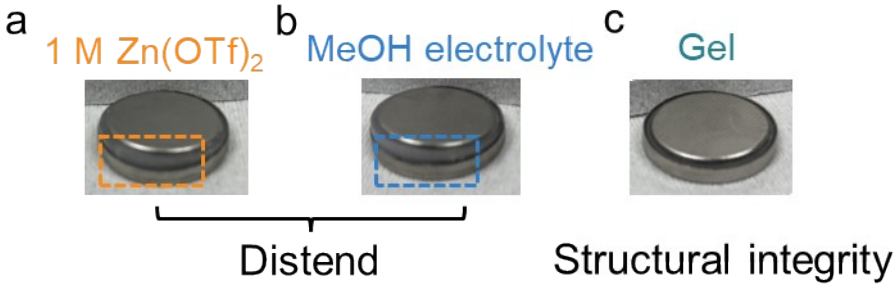

Fig. S20. Optical photographs of ZMB cells assembled with (a) 1 M $Zn(OTf)_2$, (b) MeOH electrolyte and (c) gel electrolyte after 6 h of storage at +60 °C. When cells containing different electrolytes were stored under +60 °C, the cells with the 1 M $Zn(OTf)_2$ and MeOH electrolyte distended, while the gel electrolyte-based cell remained structural integrity.

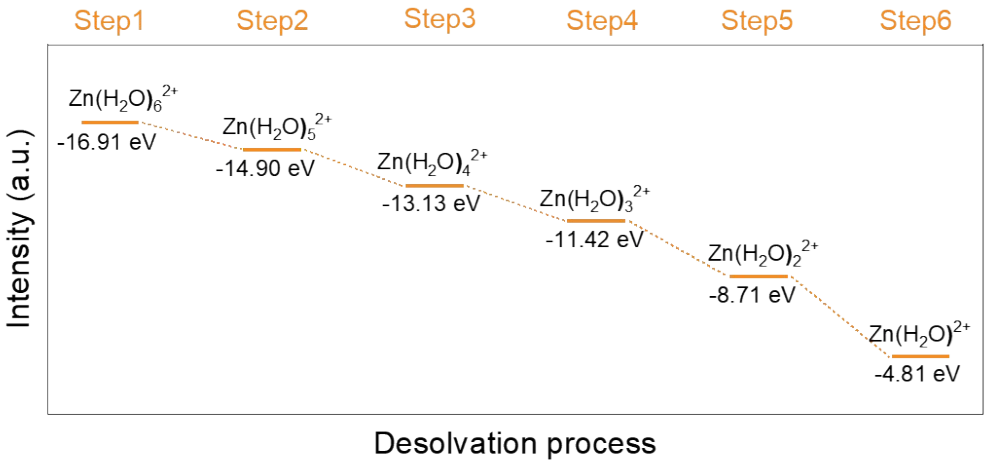

Fig. S21. The proposed desolvation process of $Zn(H_2O)_6^{2+}$. In contrast, the desolvation process of $Zn(H_2O)_6^{2+}$ brings active water molecules to the electrode|electrolyte interface, promoting water-related decomposition reactions at the interface.

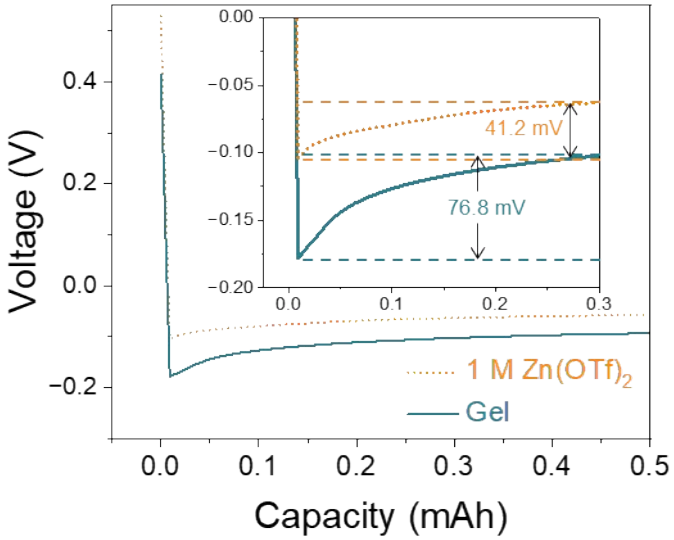

Fig. S22. Nucleation overpotential of Zn plating within (a) 1 M $Zn(OTf)_2$ aqueous electrolyte and (b) gel electrolyte.

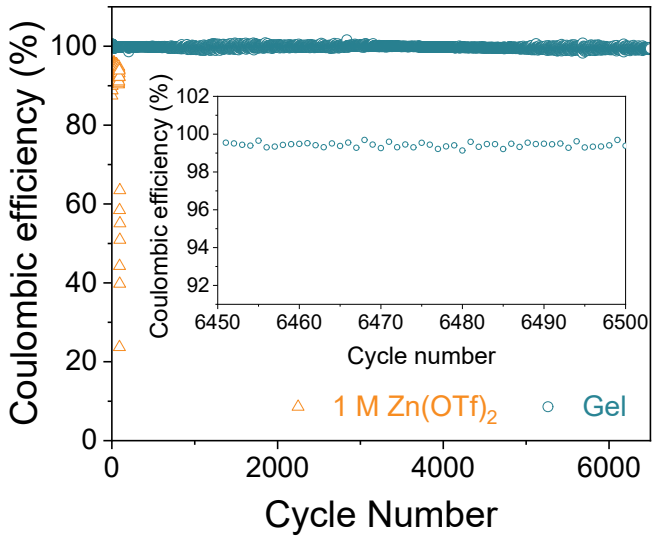

Fig. S23. Cycle performance of Zn||Cu asymmetric cells with different electrolytes at 1 cm^{-2} and 0.5 mAh cm^{-2}. The inset is an enlarged view of a Zn||Cu asymmetric cell assembled with gel electrolyte at the last 50 cycles.

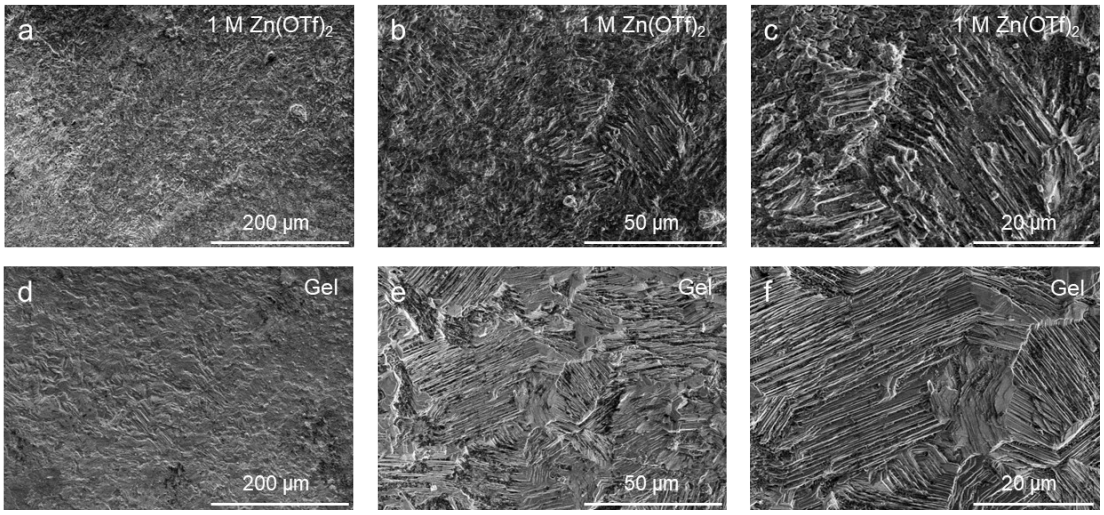

Fig. S24. Top-view SEM images of Zn deposition morphologies in (a-c) 1 M $Zn(OTf)_2$ aqueous electrolyte and (d-f) gel electrolyte.

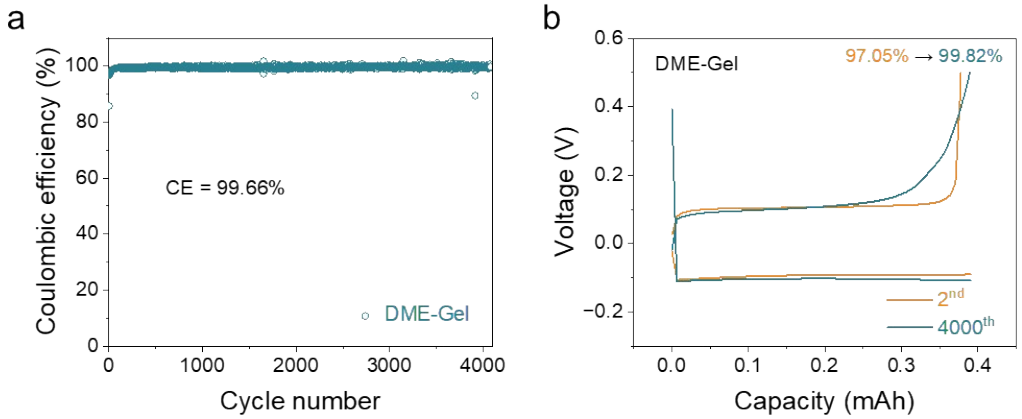

Fig. S25. (a) Cycle performance and (b) typical voltage profiles of Zn||Cu cells at 1 mA cm^{-2} and 0.5 mAh cm^{-2} in DME-based gel electrolyte.

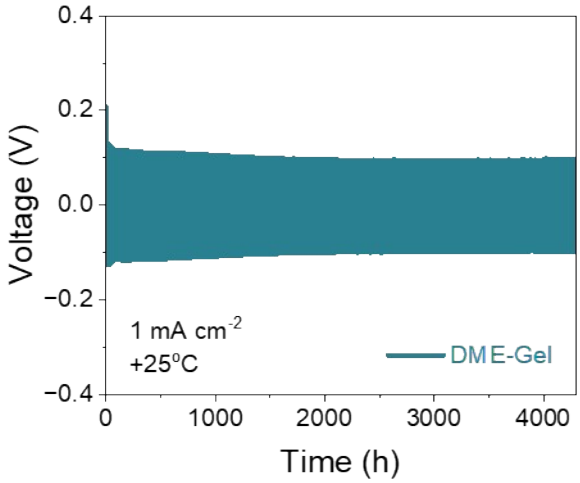

Fig. S26. Long-term cycle performance of Zn||Zn symmetric cells with DME-based gel electrolyte at 1 mA cm^{-2} and 1 mAh cm^{-2} at 25 °C.

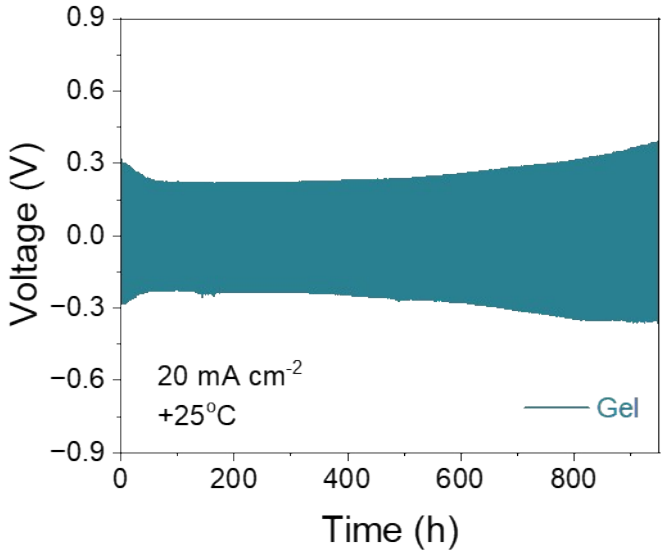

Fig. S27. Long-term cycle performance of Zn||Zn symmetric cells with gel electrolyte at 20 mA cm^{-2} and 20 mAh cm^{-2}.

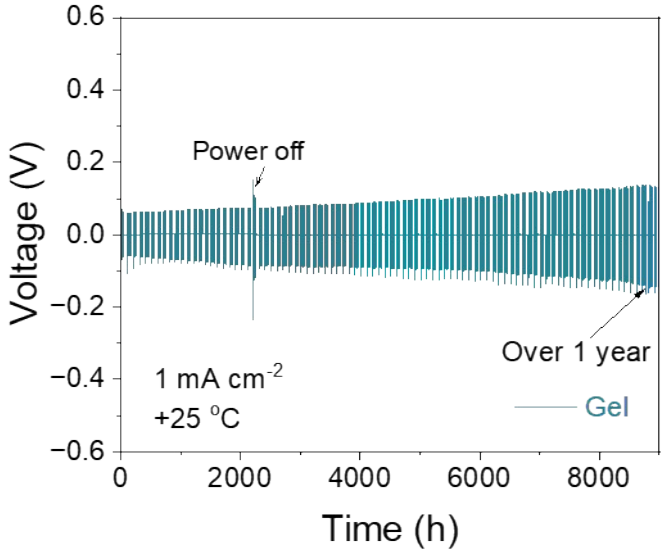

Fig. S28. Shelving-recovery performance of Zn||Zn symmetric cells with gel electrolyte at 1 mA cm^{-2} and 1 mAh cm^{-2}.

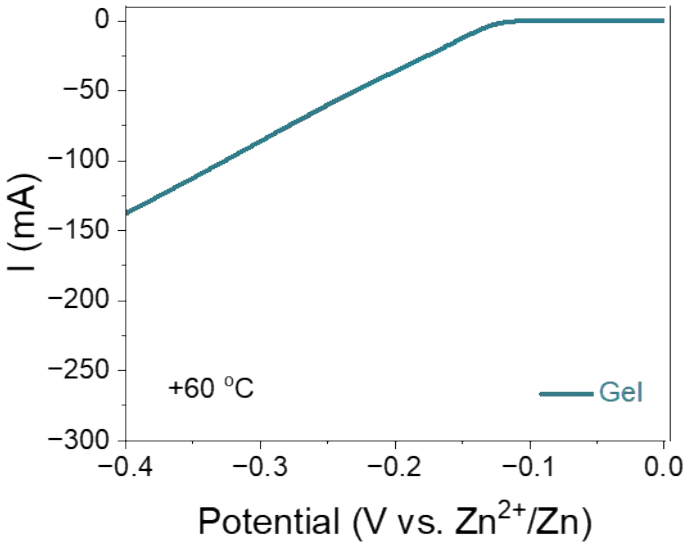

Fig. S29. LSV curves in gel electrolyte at +60 °C.

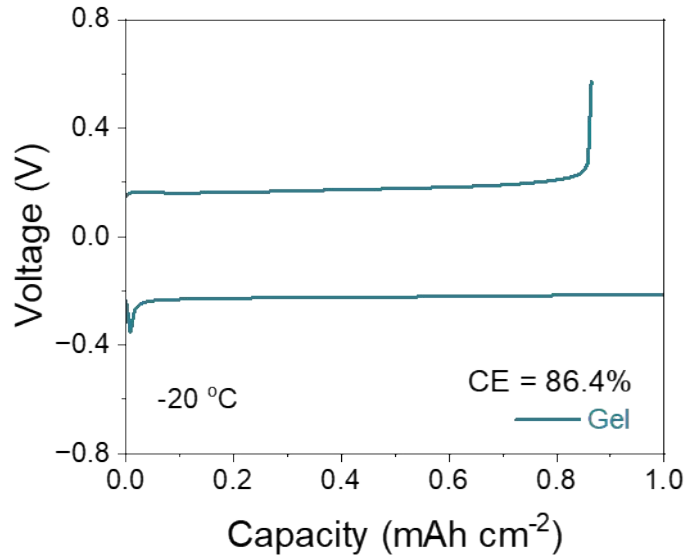

Fig. S30. Initial charge-discharge curve of Zn||Cu cell assembled within gel electrolyte at -20 °C.

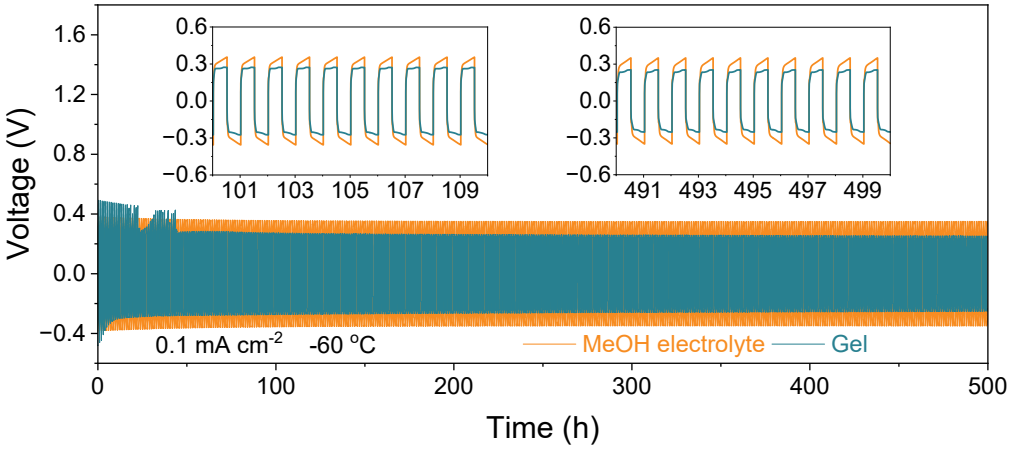

Fig. S31. Long-term cycle performance of Zn||Zn symmetric cells with MeOH electrolyte and gel electrolyte at −60 °C and 0.1 mA cm^{-2}.

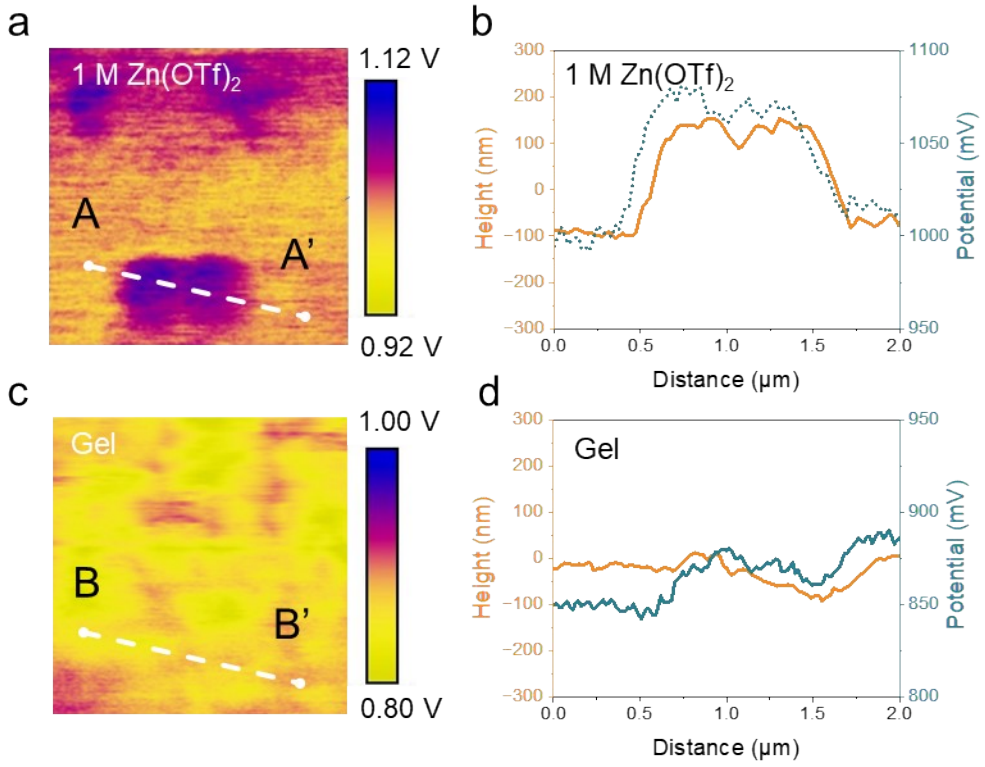

Fig. S32. (a, c) Contact potential difference (CPD) maps and (b, d) line profiles taken from the KPFM images for the Zn deposition layer on Cu foil in (a, b) 1 M Zn(OTf)$_2$ aqueous electrolyte and (c, d) gel electrolyte. The scan size is 3 μm × 3 μm. A smoother Zn surface with a more uniform distribution of the CPD) and surface height was observed in the gel electrolyte compared to those in aqueous electrolyte.

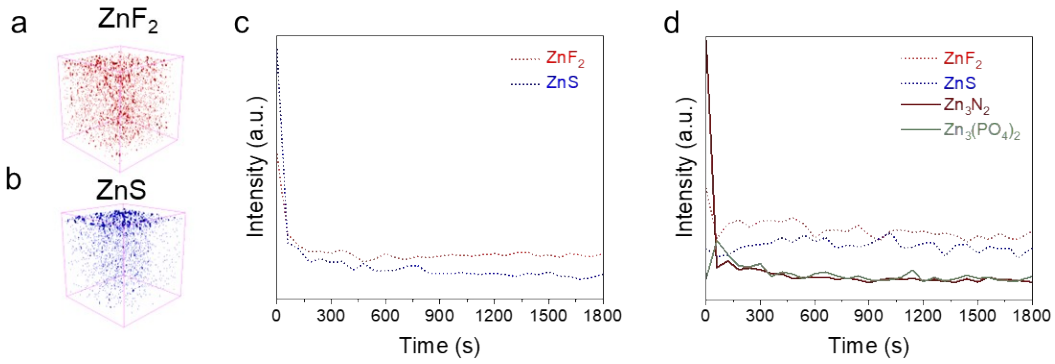

Fig. S33. (a, b) Spatial distributions on the cycled Zn anodes from 1 M $Zn(OTf)_2$ aqueous electrolyte and depth profiles from (c) 1 M $Zn(OTf)_2$ aqueous electrolyte and (d) gel electrolyte over 1800s etching time for the Zn anode after 50 cycles.

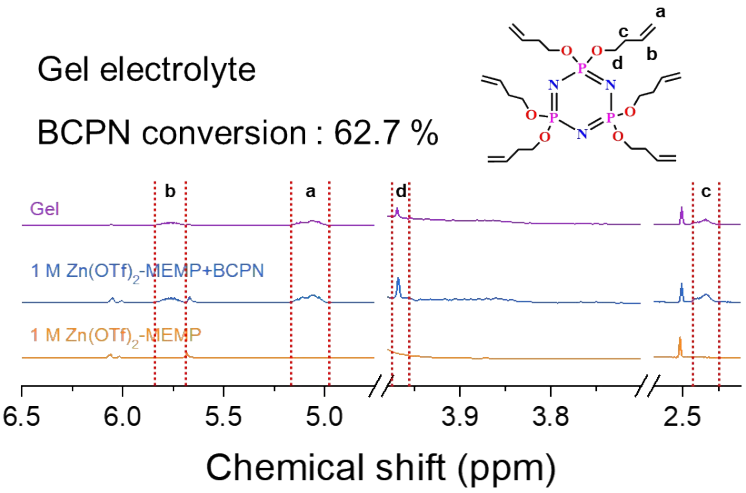

Fig. S34. ^1H NMR spectra of 1 M $Zn(OTf)_2$-1 wt% MEMP; 1 M $Zn(OTf)_2$-1 wt% MEMP with 5wt% BCPN, and gel electrolyte. The conversion degree of BCPN monomer in the gel electrolyte was identified as 62.7%.

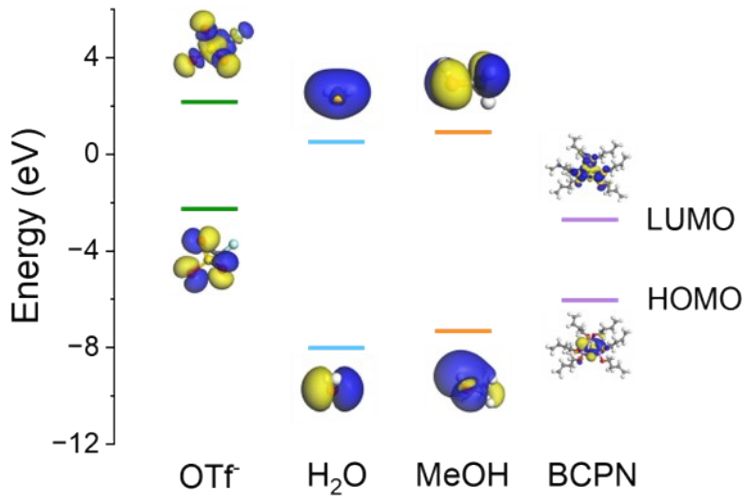

Fig. S35. The lowest unoccupied molecular orbital (LUMO) and the highest occupied molecular orbital (HOMO) energy values of OTf^-, H_2O, MeOH and BCPN molecules. The corresponding molecular structures are shown in the insets. Color code: O, red; F, cyan; C, dark gray; S, yellow, N, dark blue; P, pink and H, white. The LUMO value of the BCPN molecule (-2.71 eV) is significantly lower than that of MeOH (0.92 eV) and H_2O (0.52 eV), suggesting that BCPN is preferentially reduced on the Zn anode to form SEI.

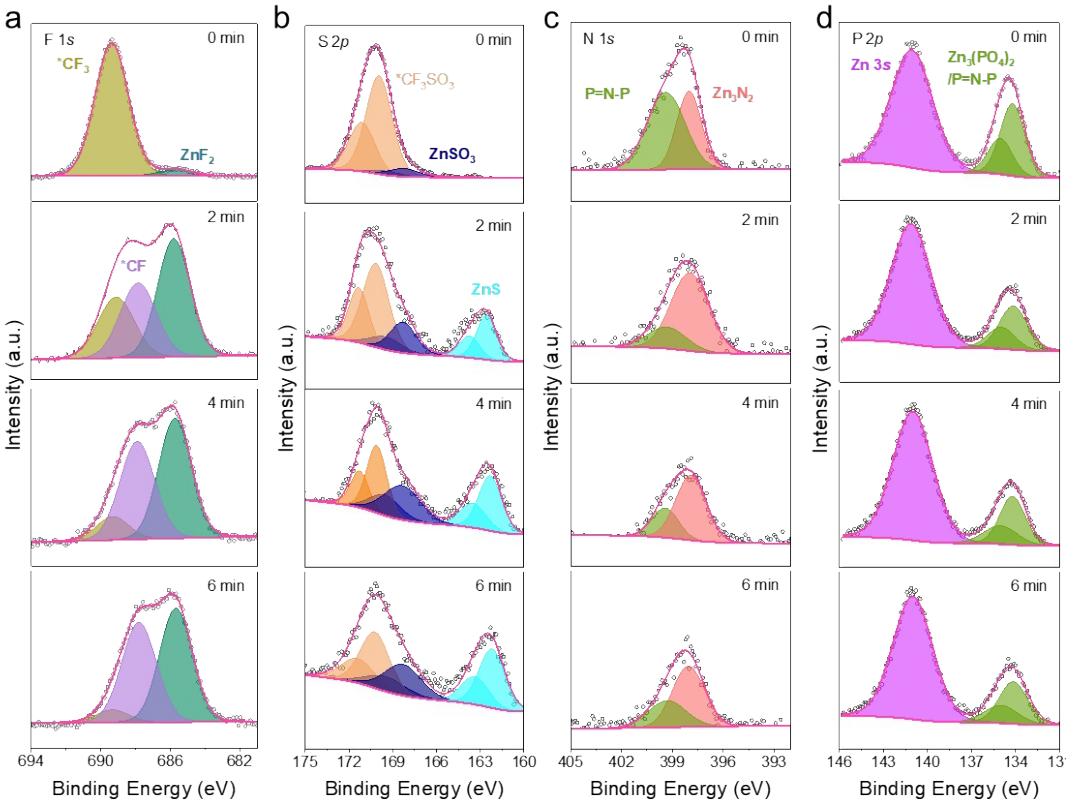

Fig. S36. High-resolution depth profiling of (a) F 1*s*, (b) S 2*p*, (c) N 1*s* and (c) P 2*p* XPS spectra of Zn foils after 30 cycles at 1 mA cm^{-2} (1 mAh cm^{-2}) in the gel electrolyte. In the F 1*s* and S 2*p* spectra, the signal intensities of ZnF_2 (~685.7 eV) and ZnS (~162.4 eV) remained almost unchanged (**Fig. S36**a, b), indicating their uniform distribution within the SEI.[6-7] Meanwhile, in the N 1*s* and P 2*p* spectra, the signal intensities of Zn_3N_2 (~397.9 eV) and $Zn_3(PO_4)_2$ (~134.2 eV) were notably higher at the top of the SEI (particularly for Zn_3N_2). This results in a passivation layer with high ionic conductivity and electronic insulation properties (**Fig. S36**c, d).[1,8-9]

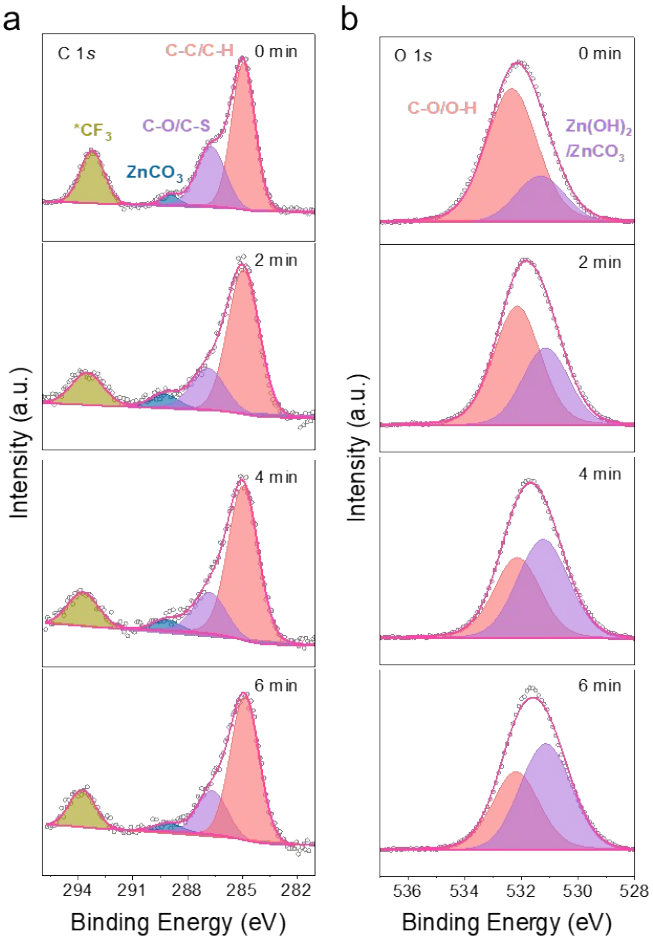

Fig. S37. High-resolution depth profiling of (a) C 1*s* and (b) O 1*s* XPS spectra of Zn foils after 30 cycles at 1 mA cm^{-2} (1 mAh cm^{-2}) in the gel electrolyte. The C 1*s* and O 1*s* spectra show an enriched SEI layer containing $Zn(OH)_2$ (~531.2 eV) and organic compounds (e.g., $Zn(CO_3)_2$ at ~298.2 eV and CH_2OC-), which are the products of MeOH decomposition. These components contribute to a more uniform deposition of Zn^{2+} ions and increase the flexibility of the SEI layer.[10-11]

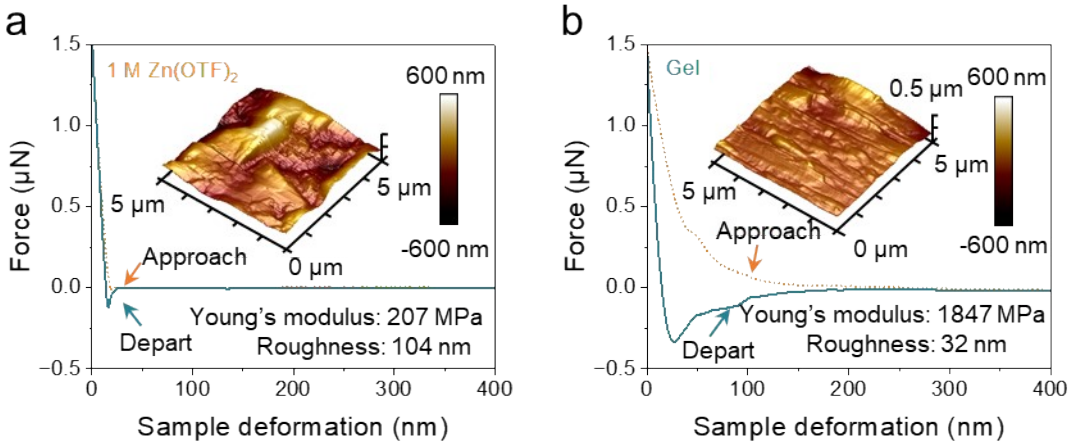

Fig. S38. Force-displacement curves of the SEI derived from (a) 1 M $Zn(OTf)_2$ aqueous electrolyte and (b) gel electrolyte. The corresponding 3D AFM scanning images of the SEI are shown in the insets.

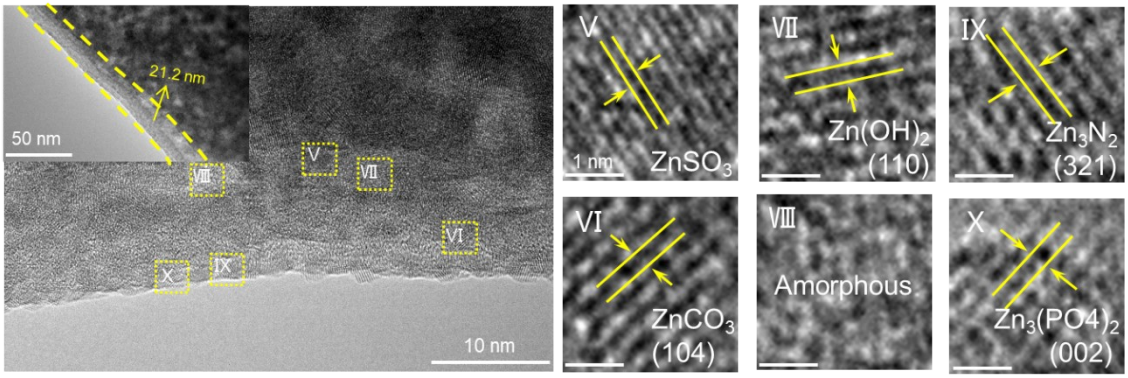

Fig. S39. HR-TEM images of the interphases on the Zn surface from gel electrolyte.

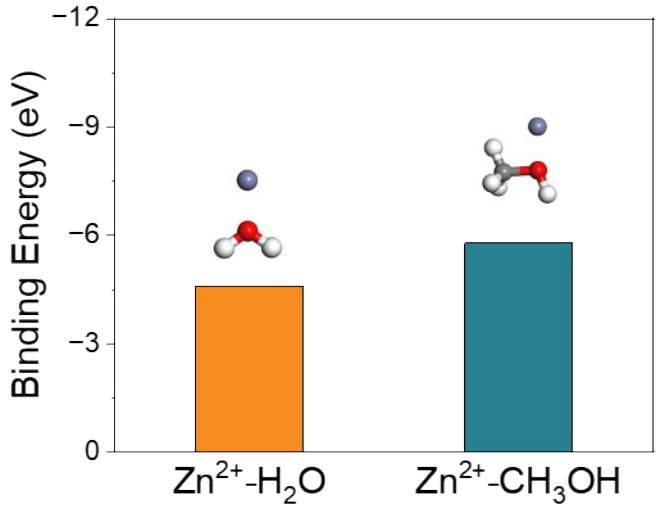

Fig. S40. Calculated binding energies between cation and different solvents. Color code: O, red; C, dark gray; and H, white.

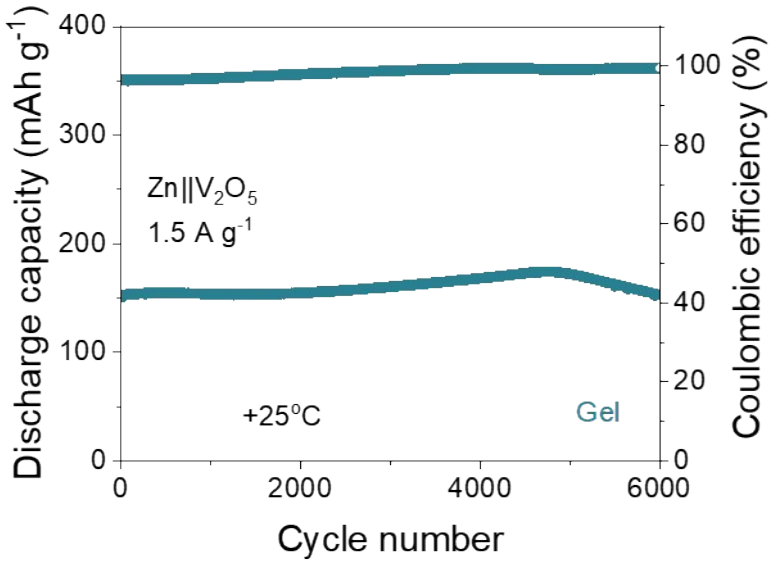

Fig. S41. Cycling performance of Zn|gel electrolyte|V_2O_5 full cell at 1.5 A g^{-1} and 25 °C. Compared to the highest discharge capacity (174.2 mAh g^{-1}), the cell with gel electrolyte maintained 87.7% capacity after 6000 cycles (152.9 mAh g^{-1}).

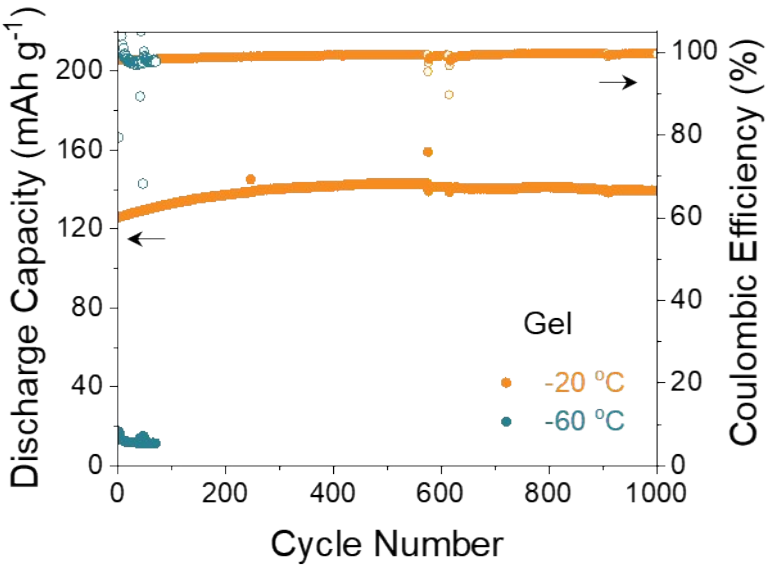

Fig. S42. Cycling performance of Zn|gel electrolyte|VOH full cells at -20 °C and -60 °C. The Zn||VOH full cells undergo room-temperature activation treatment prior to low-temperature cycling. At -20 °C, the Zn|gel electrolyte|VOH cell maintained 97.27% capacity after 1000 cycles (139.2 mAh g^{-1}). However, at -60 °C, the the Zn|gel electrolyte|VOH cell showed almost no capacity utilization.

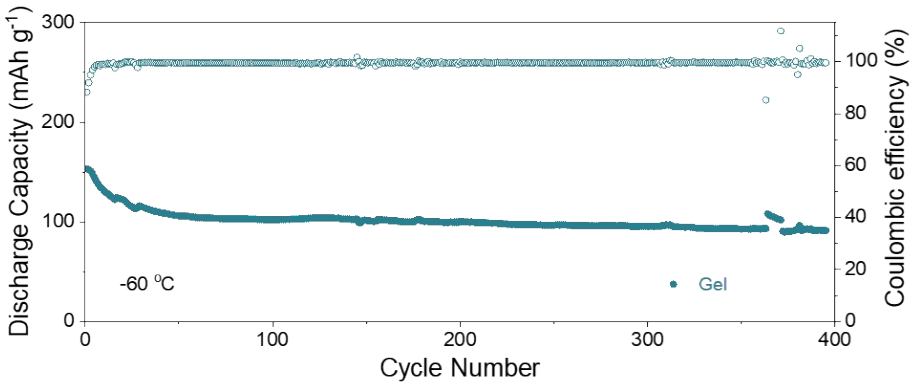

Fig. S43. Cycling performance of Zn||PANI full cell with gel electrolyte at -60 °C.

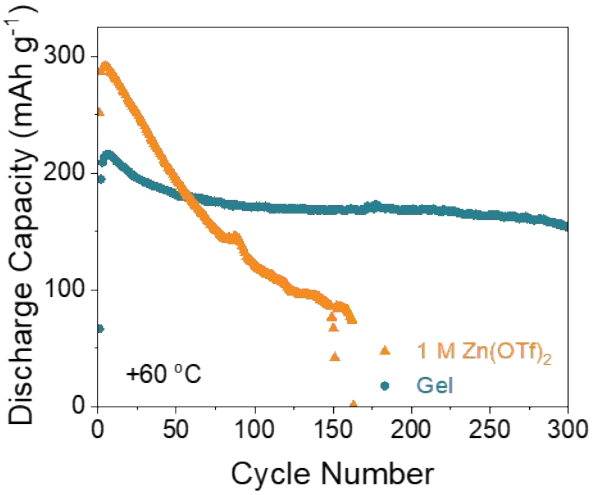

Fig. S44. Cycling performance of Zn||VOH full cells with different electrolytes at +60 °C.

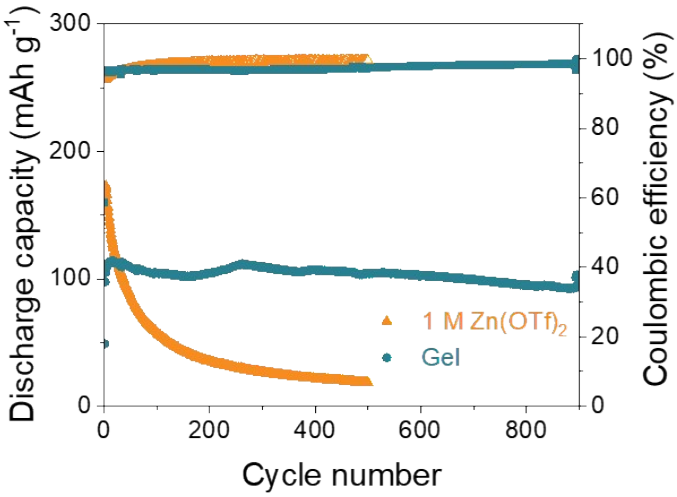

Fig. S45. Cycling performance of Zn||VOH pouch cells with different electrolytes at 1.5 A g^{-1}.

Table S1. Performance comparison of Zn||Cu cells in this work with previous reports.

Electrolyte	Cycle number	Average coulombic efficiency (%)	Cumulative deposition capacity (mAh cm^{-2})	Ref
Gel	6500	99.75	3250	This work
FDHE	1000	99.1	2500	12
Sor-cel	200	99.6	400	13
DCZ-gel	2000	99.4	2000	14
CL	500	99.7	1250	15
TEDA	1720	98.7	1720	16
PAM/Tre	850	98.8	1700	17
PDMAPS	500	99.32	500	18
SCH	500	99.6	2000	19
PAM-1,2-PG	3700	99.1	1480	20
PEGDA	2900	99.66	1450	21
PCD-20	250	99.1	250	22
PDZ	330	99.5	1320	23

Table S2. Performance comparison of Zn||PANI cells in this work with previous reports at LT.

Electrolyte	Low temperature (°C)	Discharge Capacity (mAh g^{-1})	Ref
Gel	-70	95.6	This work
Gel	-60	153.4	This work
PAM	-70	45.2	24
3ZC6LC	-50	96.5	25
Z6S	-40	76	26
Sor-cel	-40	63	13
PAGE	-35	152.4	27
CSAM-C	-30	123	28
AF-SH-CPAM	-20	160.3	29
QDP	-20	49.7	30
FDHE	-10	124	12

References

1 Y. Meng, D. Zhou, R. Liu, Y. Tian, Y. Gao, Y. Wang, B. Sun, F. Kang, M. Armand, B. Li, G. Wang and D. Aurbach, *Nat. Energy*, 2023, **8**, 1023-1033.

2 L. Dong, H. J. Yan, Q. X. Liu, J. Y. Liang, J. Yue, M. Niu, X. Chen, E. Wang, S. Xin, X. Zhang, C. Yang and Y. G. Guo, *Angew. Chem., Int. Ed.*, 2024, **136**, e202411029.

3 R. Han, Z. Wang, D. Huang, F. Zhang, A. Pan, H. Song, Y. Wei, Y. Liu, L. Wang, Y. Li, J. Xu, J. Hu and X. Wu, *Small*, 2023, **19**, 2300571.

4 Z. Wang, H. Zhang, J. Xu, A. Pan, F. Zhang, L. Wang, R. Han, J. Hu, M. Liu and X. Wu, *Adv. Funct. Mater.*, 2022, **32**, 2112598.

5 Y. Zhong, X. Xie, Z. Zeng, B. Lu, G. Chen and J. Zhou, *Angew. Chem., Int. Ed.*, 2023, **62**, e202310577.

6 X. Zhao, Y. Wang, C. Huang, Y. Gao, M. Huang, Y. Ding, X. Wang, Z. Si, D. Zhou and F. Kang, *Angew. Chem., Int. Ed.*, 2023, **62**, e202312193.

7 X. Zhao, J. Fu, M. Chen, Y. Wang, C. Huang, K. Qian, G. Feng, B. Li, D. Zhou and F. Kang, *J. Am. Chem. Soc.*, 2025, **147**, 2714-2725.

8 X. Guo, J. Lu, M. Wang, A. Chen, H. Hong, Q. Li, J. Zhu, Y. Wang, S. Yang, Z. Huang, Y. Wang, Z. Pei and C. Zhi, *Chem*, 2024, **10**, 3607-3621.

9 W. Wang, S. Chen, X. Liao, R. Huang, F. Wang, J. Chen, Y. Wang, F. Wang and H. Wang, *Nat. Commun.*, 2023, **14**, 5443.

10 W. Xu, J. Li, X. Liao, L. Zhang, X. Zhang, C. Liu, K. Amine, K. Zhao and J. Lu, *J. Am. Chem. Soc.*, 2023, **145**, 22456-22465.

11 L. Ma, J. Vatamanu, N. T. Hahn, T. P. Pollard, O. Borodin, V. Petkov, M. A. Schroeder, Y. Ren, M. S. Ding, C. Luo, J. L. Allen, C. Wang and K. Xu, *P. Natl. Acad. Sci. Usa*, 2022, **119**, e2121138119.

12 Y. Liu, H. He, A. Gao, J. Ling, F. Yi, J. Hao, Q. Li and D. Shu, *Chem. Eng. J.*, 2022, **446**, 137021.

13 Y. Quan, W. Zhou, T. Wu, M. Chen, X. Han, Q. Tian, J. Xu and J. Chen, *Chem. Eng. J.*, 2022, **446**, 137056.

14 H. Zhang, X. Gan, Y. Yan, J. Zhou, *Nano-Micro Lett.*, 2024, **16**, 106.

15 X. Shi, C. Dong, L. Ma, M. Yang, X. Chen, Y. Zhang, L. Liu, Z. Long, *Chem. Eng. J.*, 2025, **504**, 158659.

16 J. Cui, Z. Tao, J. Wu, S. Ma, Y. Yang, J. Zhang, *Small*, 2023, **19**, 2304640.

17 S. Yang, Q. Wu, Y. Li, F. Luo, J. Zhang, K. Chen, Y. You, J. Huang, H. Xie, Y. Chen, *Angew. Chem., Int. Ed.,* 2024, **63**, e202409160.

18 S. Zhang, H. A. Ao, J. Dong, D. Wang, C. Wang, X. Xu, Z. Hou, J. Yang, *Angew. Chem., Int. Ed.,* 2025, **64**, e202414702.

19 X. Luo, Q. Nian, Q. Dong, D. Ruan, Z. Cui, Z. Wang, B. Q. Xiong, X. Ren, *Adv. Energy Mater.*, 2024, **15**, 2403187.

20 S.-J. Guo, M.-Y. Yan, D.-M. Xu, P. He, K.-J. Yan, J.-X. Zhu, Y.-K. Yu, Z.-Y. Peng, Y.-Z. Luo, F.-F. Cao, *Energ. Environ. Sci.*, 2025, **18**, 418-429.

21 J. Zhao, C. Song, S. Ma, Q. Gao, Z. Li, Y. Dai, G. Li, *Energy Storage Mater.*, 2023, **61**, 102880.

22 S. Huang, S. He, Y. Li, S. Wang, X. Hou, *Chem. Eng. J.*, 2023, **464**, 142607.

23 H. Lu, J. Hu, L. Wang, J. Li, X. Ma, Z. Zhu, H. Li, Y. Zhao, Y. Li, J. Zhao, B. Xu, *Adv. Funct. Mater.*, 2022, **32**, 2112540.

24 Y. Shi, R. Wang, S. Bi, M. Yang, L. Liu and Z. Niu, *Adv. Funct. Mater.*, 2023, **33**, 2214546.

25 C. Yan, Y. Wang, X. Deng and Y. Xu, *Nano-Micro Lett.*, 2022, **14**, 98.

26 X. Lin, G. Zhou, M. J. Robson, J. Yu, S. C. T. Kwok and F. Ciucci, *Adv. Funct. Mater.*, 2021, **32**, 2109322.

27 D. Feng, Y. Jiao and P. Wu, *Angew. Chem., Int. Ed.*, 2022, **62**, e202215060.

28 S. Huang, L. Hou, T. Li, Y. Jiao and P. Wu, *Adv. Mater.*, 2022, **34**, 2110140.

29 X. Jin, L. Song, C. Dai, H. Ma, Y. Xiao, X. Zhang, Y. Han, X. Li, J. Zhang, Y. Zhao, Z. Zhang, L. Duan and L. Qu, *Energy Storage Mater.*, 2022, **44**, 517-526.

30 J. Du, X. Zhan, Y. Xu, K. Diao, D. Zhang and S. Qin, *J. Mater. Sci. Technol.*, 2025, **212**, 251-258.